Negative Permittivity in $(V_2O_5)_{100-x}Se_x$ Alloys

Sandeep Kohli,* Christopher D. Rithner, and Peter K. Dorhout

Department of Chemistry, Colorado State University, Fort Collins, Colorado 80523

Received November 27, 2001. Revised Manuscript Received July 12, 2002

$(V_2O_5)_{100-x}Se_x$ (x = 9, 17, 25, 30 wt %) alloys have been prepared by quenching the melt from 1000 to 273 K in ice water. The XRD data show the presence of crystalline V_2O_5, V_6O_{13}, VO_2, and Se phases. High-resolution XPS spectra for a Se 3d peak show the presence of SeO_2 and elemental Se phases in the samples. The presence of a reversible endothermic peak ≈343 K in the differential scanning calorimetric (DSC) curve of quenched samples is indicative of the monoclinic to tetragonal transformation in VO_2. A selenium melting peak at 495 K is also present in the DSC curve, for $x \geq 17$. Room-temperature dielectric measurements in the frequency range 1 Hz to 100 kHz show the presence of negative permittivity in samples with $x < 30$. Permittivity Vs temperature and loss-factor Vs temperature measurements in the temperature range 273−373 K and at a fixed frequency of 1 kHz were reversible with hysteresis across the monoclinic to tetragonal transformation of VO_2. A sample with $x = 30$ exhibits a minimum temperature range of hysteresis and large change in the value of permittivity. The diffuse reflectivity values for the sample decreases with the increased selenium content until $x \leq 17$. For $x > 17$, the reflectivity of the samples increases with increased selenium content. This is explained in terms of the increased V_2O_5 component in the samples.

Introduction

The ability of vanadium to exist in different oxidation states with different physical properties has been the subject of various studies in the past for scientific and technological applications. Both VO_2 and V_2O_5 are among the most studied compounds in the V−O system.[1] V_2O_5 has been investigated for its application in electrochromic devices, oxidation catalysis, and optical switches.[2−5] VO_2, with an optical band gap of 2.6 eV, undergoes monoclinic semiconducting, to tetragonal metallic phase transition at 341 K, accompanied by abrupt changes in the electrical, optical, and magnetic properties across the transition.[2,6] VO_2 has been studied for its application in temperature sensing devices,[7] optical switching devices,[8] modulators and polarizers of submillimeter wave radiation,[9] optical data storage media,[10] and variable reflectance mirrors.[11]

In the literature the appearance of negative capacitance[12−17] and negative permittivity[18] has been reported for materials such as a-Se,[12] nanocrystalline WO_3,[19] a-$Ge_7Si_{14}Te_{32}As_{36}Ga_{11}$,[20] and zeolites.[17] Large numbers of these reports have been devoted mainly to the electrical characterization of these samples, with insufficient data reported on the other structural and optical properties of these materials. To our knowledge, no attempt has also been made to tailor the negative capacitance/permittivity in the samples. In the past, negative capacitance has been reported in thin film Al−V_2O_5−Al devices[21] and amorphous V_2O_5 films.[22] To the best of our knowledge, there are no reports on the presence of negative capacitance or permittivity in VO_2 or V_6O_{13}. We report here the appearance of negative permittivity in $(V_2O_5)_{100-x}Se_x$ alloys, which have been well characterized for their structure, chemical, thermal, electrical, and optical properties.

In the present studies, the $(V_2O_5)_{100-x}Se_x$ (x = 9, 17, 25, 30 wt %) alloys have been prepared by quenching a melt of V_2O_5 and selenium from 1000 to 273 K in ice water. Samples have been characterized by powder

* To whom correspondence should be addressed. E-mail: skohli@lamar.colostate.edu.

(1) Moshfegh, A. Z.; Ignatiev, A. *Thin Solid Films* **1991**, *198*, 251.
(2) Barreca, D.; Depero, L. E.; Franzato, E.; Rizzi, G. A.; Sangaletti, L.; Tondello, E.; Vettori, U. *J. Electrochem. Soc.* **1999**, *146*, 551.
(3) Park, H. K.; Smyrl, W. H.; Ward, M. D. *J. Elecrochem. Soc.* **1995**, *142*, 1068.
(4) Aita, C. R.; Liu, Y.-L.; Kao, M. L. *J. Appl. Phys.* **1986**, *60*, 749.
(5) Busca, G.; Ramis, G.; Lorenzelli, V. *J. Mol. Catal.* **1989**, *50*, 231.
(6) Rogers, K. D.; Coath, J. A.; Lovell, M. C. *J. Appl. Phys.* **1991**, *70*, 1412.
(7) Takahashi, Y.; Kanamori, M.; Hashimoto, H.; Moritani, Y.; Masuda, Y. *J. Mater. Sci.* **1989**, *24*, 192.
(8) Chain, E. E. *Appl. Opt.* **1991**, *30*, 2782.
(9) Fan, J. C. C.; Fetterman, H. R.; Bachner, F. J.; Zavrasky, P. M.; Parker, C. D. *Appl. Phys. Lett.* **1977**, *30*, 11.
(10) Balberg, I.; Trokman, S. *J. Appl. Phys.* **1975**, *46*, 2111.
(11) Razavi, A.; Huges, T.; Antinovich, J.; Hoffman, J. *J. Vac. Sci. Technol. A* **1989**, *7*, 1310.
(12) Vogel, R.; Walsh, P. J. *Appl. Phys. Lett.* **1969**, *216*, 7.
(13) Nikitas, P. *Electrochim. Acta* **1992**, *37*, 81.
(14) Beale, M.; Mackay, P. *Philos. Mag. B* **1992**, *65*, 47.
(15) Stapelton, S. P.; Deen, M. J.; Berolo, E.; Hardy, R. H. S. *Electron. Lett.* **1990**, *26*, 84.
(16) Beale, M. *Philos. Mag. B* **1993**, *68*, 573.
(17) Fernandez, F. G.; Gonzalez, E.; Berazain, A.; Hernandez, M. V. *Proceedings of the 5th IEEE International conference on Conduction Breakdown in Solid Dielectrics, Leicester, UK*; IEEE: New York, 1995; p 3730.
(18) M'Peko, J.-C. *Appl. Phys. Lett.* **1997**, *71*, 3730.
(19) Hoel, A.; Kish, L. B.; Vajtai, R.; Niklasson, G. A.; Granqvist, C. G.; Olsson, E. *Mater. Res. Soc. Symp. Proc.* **2000**, *581*, 15.
(20) Allen, M.; Walsh, P.; Doremus, W. Negative Capacitance Effect in Amorphous Semiconductor. *Phys. Electron. Ceram., Proc. Electron. Phenomena Ceram. Conf.*; Hench, L. L., Ed.; Dekker: New York, 1971; Part A, p 269.
(21) Bhosle, S. A.; Nadkarni, G. S.; Radhakrishnan, S. *Phys. Status Solidi A* **1987**, *101*, 639.
(22) Thomas, B.; Jayalekshmi; S. *J. Non-Cryst. Solids* **1989**, *113*, 65.

10.1021/cm011574l CCC: $22.00
Published on Web 08/24/2002

X-ray diffraction (XRD), X-ray photoelectron spectroscopy (XPS), differential scanning calorimetric (DSC) studies, dielectric analysis (DEA), and diffuse reflectance measurements.

Experimental Section

Bulk samples of $(V_2O_5)_{100-x}Se_x$ (x = 9, 17, 25, 30 wt %) have been prepared by a conventional melt-quenching technique.[23] V_2O_5 and Se (99.9%) were weighed accordingly and sealed in a vacuum of 10^{-3} Pa in quartz ampules. The samples were then heated to a temperature of 1000 K for 24 h and quenched in ice water. The ampules were rocked during the heating process to ensure mixing of the constituents. Powder X-ray diffraction studies, for structural investigation, were performed using the calibrated Bruker D-8 Discover (Cu Kα_1, λ = 1.5406 Å) with a Göbel mirror on the primary beam side and scintillation detector on the diffracted beam side. XRD spectra were collected with a step size of 0.01° and time per step of 2 s over the 2θ range 10°−90°. The diffraction system was calibrated using standard quartz peaks. More details of the X-ray diffraction instrument are published elsewhere.[24]

X-ray photoelectron spectroscopic measurements were performed using a Physical Electronics 5800 Model. A monochromatic Al Kα line of energy, 1486.6 eV, was employed as an X-ray source. An initial survey scan (pass energy = 93.90 eV, eV/step = 0.80, time/step = 30 ms) was done for the identification of the elemental species. Integrated peak area intensities under V 2p and Se 3d peaks were used for estimating the selenium content in the samples. The integrated peak area was normalized with respect to each core level atomic sensitivity factor.[25] High-resolution scans for V 2p and Se 3d were performed with a pass energy of 23.50 eV and step size of 0.025 eV. Spectra for the Se 3d peak were collected for 30 cycles while those for V 2p for 10 cycles were collected due to the low intensity of the Se 3d peak relative to that of the V 2p peak. The background pressure during measurements was lower than 2×10^{-7} Pa.

Differential scanning calorimetric (DSC) measurements were performed on the samples using a calibrated TA2920 MDSC (TA Instruments) with a low-temperature accessory. The DSC cell was purged continuously with nitrogen (60 cm^3/min) during the experiments. The DSC cell was calibrated for baseline and temperature.[26] Weighed samples were hermetically sealed in Al pans and heated at 15 K/min.

Room-temperature dielectric measurements in the frequency range 1 Hz to 100 kHz, using an applied voltage of 1.0 V, were performed with a TA Instruments dielectric analyzer (DEA, 2970) for the estimation of permittivity and loss factor. Gold-coated ceramic plate parallel sensors were used for the measurements. The diameter of the gold-coated region was 25 mm.[27] The electrodes transmitted an applied oscillating voltage to the sample and measured the response of the sample to the applied voltage. The powder samples were compressed in the form of disks and placed between the excitation and response electrodes. A force of 250 N was applied from the upper electrode assembly to ensure good contact between the sample and electrodes, thus minimizing noise. A linear variable displacement transducer (LVDT) was used to accurately measure the sample thickness. Ceramic parallel plate sensors featured a guard ring on the response electrode that minimized the effect of fringing fields and reduced noise in the loss factor data. The excitation electrode contained a platinum resistance thermistor, which was in direct contact with the sample and provided accurate temperature measurements.[28] The difference in the area of sample and electrode was taken into consideration for the presentation of data. The DEA cell was purged with dry nitrogen (60 cm^3/min) for 1 h before the start of measurements and also during experiments. The low-temperature accessory was used to measure the dielectric response as a function of temperature in the range 273−373 K at a fixed frequency of 1 kHz.

Diffuse reflectance measurements in the wavelength range 250−1000 nm were performed using a double-beam Cary 500 (Varian Analytical) spectrophotometer fitted with a praying mantis to analyze powdered samples. Compressed PTFE was used for the standard calibration.

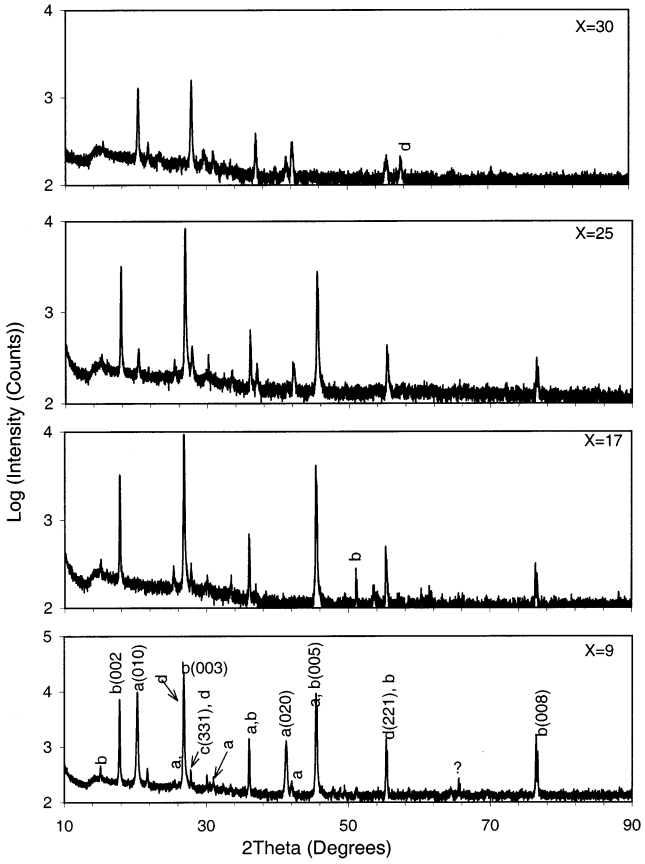

Figure 1. XRD spectra for melt-quenched $(V_2O_5)_{100-x}Se_x$ samples. Miller indices for some peaks are shown. (a) V_2O_5,[30] (b) V_6O_{13},[31] (c) Se,[32] and (d) VO_2.[33] Intensity (counts) was plotted on a log scale for the clarity of presentation of peaks with low relative intensity.

Results and Discussion

X-ray Diffraction. Figure 1 shows the X-ray diffraction pattern of the $(V_2O_5)_{100-x}Se_x$ samples. The crystalline peaks in the X-ray diffraction pattern for the samples were compared against the standard in the ICDD database using search-match software provided by Bruker[29] following background subtraction. Search-match results indicated the presence of orthorhombic V_2O_5,[30] monoclinic V_6O_{13},[31] elemental Se,[32] and VO_2[33] phases in the melt-quenched samples. The ratio of the phases V_2O_5/V_6O_{13} decreased with the increase of selenium content until x = 17; between x = 17 and x = 30

(23) Mehra, R. M.; Kohli, S.; Pundir, A.; Sachdev, V. K.; Mathur, P. C. *J. Appl. Phys.* **1997**, *81*, 7842.
(24) Kohli, S.; Rithner, C. D.; Dorhout, P. K. *J. Appl. Phys.* **2002**, *91*, 1149.
(25) Moulder, J. F.; Stickle, W. F.; Sobol, P. E.; Bomben, K. D. *Handbook of X-ray Photoelectron Spectroscopy- A Reference Book of Standard Spectra for Indentification and Interpretation of XPS Data*; Chastain, J., King, R. C., Jr., Eds.; Physical Electronics Inc.: Eden Prairie, MN, 1995.
(26) *Differential Scanning Calorimeter Operator's Manual (DSC2920)*; TA Instruments: New Castle, DE, 1998.
(27) *Dielectric Analyzer Operator's Manual (DEA2970)*; TA Instruments: New Castle, DE, 1997.
(28) *Thermal Analysis Application Brief, Number TA-142*; TA Instruments: New Castle, DE, 1997.
(29) *Diffrac^{plus} Search / match, User's Manual*; Bruker AXS GmbH: Karlsruhe, Germany, 1998.

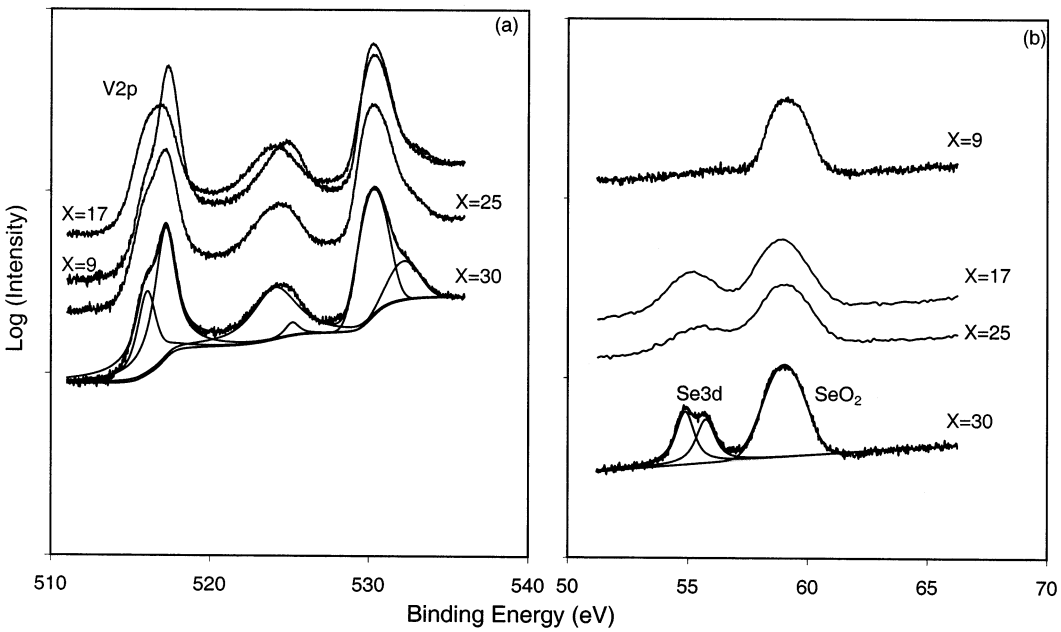

Figure 2. High-resolution XPS spectra for (a) Se 3d and (b) V 2p peak for $9 \leq x \leq 30$. The fitted curves for $x = 30$ are also shown. Intensity (a.u.) is plotted on a log scale for the sake of presentation only.

the ratio increased with increasing selenium content. It should also be noted that several peaks from different phases overlap each other, which makes the complete quantitative analysis of phase identification complicated.

X-ray Photoelectron Spectroscopic Measurements. Figure 2 shows the high-resolution XPS spectra for Se 3d and V 2p peaks for $(V_2O_5)_{100-x}Se_x$ samples. The fitted curves for $x = 30$ are also shown in the figure. The high-resolution spectra for Se 3d and V 2p peaks were profile-fitted using XPSPEAK Version 4.1 software.[34] As seen in Figure 2, the fitted curve for Se 3d shows the presence of elemental Se and SeO_2 with their peaks at 55.6 and 58.9 eV, respectively.[25] We also observed that the sample with $x = 30$ showed the doublet for the Se $3d_{3/2,5/2}$ peak with peak energies at 55.74 and 54.88 eV. The fitted curve for $x = 30$ shows the presence of V_2O_5 and VO_2 with peaks at 517.4 and 516.3 eV, respectively.[25] The ratio of the area under the peaks was used to estimate the ratio of Se/SeO_2 and V_2O_5/VO_2. The results are compiled in Table 1. The V/Se ratio was calculated from the integrated peak area intensities under V 2p and Se 3d peaks in the survey scan. The integrated peak area was normalized with respect to each core level atomic sensitivity factor.[25] As seen in the table, the ratio of selenium to selenium oxide increases with increasing selenium content. Although the wt % of Se in the sample where $x = 17$ increased by a factor of ≈ 2 as compared to that $x = 9$, the corresponding ratio of Se/SeO_2 increased by a factor of 8. One possible explanation for this could be the formation of a small selenium crystallite core surrounded by a thick SeO_2 skin, as compared to the size of selenium crystallite. With an increased selenium content for example, where $x > 9$, a large selenium core with thin skin, as compared to the size of selenium crystallite, was formed. The ratio of the area under the peaks for V_2O_5 and VO_2 decreased until $x = 17$; for $x > 17$ the ratio increased to $x = 30$. These results are consistent with the XRD results.

Table 1. Parameters Obtained from the XPS Measurements[a]

	Se/V	A_{Se}/A_{SeO_2}	$A_{V_2O_5}/A_{VO_2}$	$A_{SeO_2}/A_{V_2O_5}$
$x = 9$	0.07	0.05 < 0.1	0.73−0.7	0.11
$x = 17$	0.16	0.44−0.4	0.05 < 0.1	16.21
$x = 25$	0.18	0.36−0.4	0.30	3.0
$x = 30$	0.27	0.37−0.4	0.94−0.9	0.3

[a] The Se/V ratio was obtained using the XPS survey scans. A_{Se}, A_{SeO_2}, $A_{V_2O_5}$, and A_{VO_2} represent the area under the peak for Se, SeO_2, V_2O_5, and VO_2, respectively. These areas have been estimated from the high-resolution scan for the Se 3d peak (B.E. = 55.6 eV) and V 2p (B.E. = 517.6 eV).

Differential Scanning Calorimetric Studies. Figure 3 shows the DSC curve for the sample $x = 9$; a heating rate of 15 K/min for the heating and cooling cycle was used. As shown in the curve, an endothermic peak, corresponding to the monoclinic to tetragonal phase transition of VO_2, occurred at 342 K. Other exothermic (616 and 669 K) peaks correspond to the oxidation/decomposition occurring in the sample. The cooling curve for $x = 9$ shows that only the endothermic peak at 342 K was reversible. The cooled sample was subjected to another set of DSC measurements and the results are shown in the inset in Figure 3. Figure 4 shows the DSC curve for $x \geq 17$. The reversible endothermic peak at $\approx$343 K is seen in all samples. Another interesting feature is the appearance of a small endothermic peak at $\approx$495 K for $x \geq 17$, corresponding to the melting of Se (T_{mSe}). As seen in the XPS results, the elemental selenium component in $x = 9$ is very low and the sample mainly comprises SeO_2. Hence, the absence of T_{mSe} at $x = 9$ could be due to the low volume

(30) JCPDS-ICDD card no. 720433. International Centre for Diffraction Data: Newton Square, PA.
(31) JCPDS-ICDD card no. 751140. International Centre for Diffraction Data: Newton Square, PA.
(32) JCPDS-ICDD card no. 761865. International Centre for Diffraction Data: Newton Square, PA.
(33) JCPDS-ICDD card no. 760456. International Centre for Diffraction Data: Newton Square, PA.
(34) Kwok, R. M. W. *XPSPEAK Version 4.1XPS Peak Fitting Program for WIN95/98*; http://www.phy.cuhk.edu.hk/~surface/XPSPEAK, 2000.

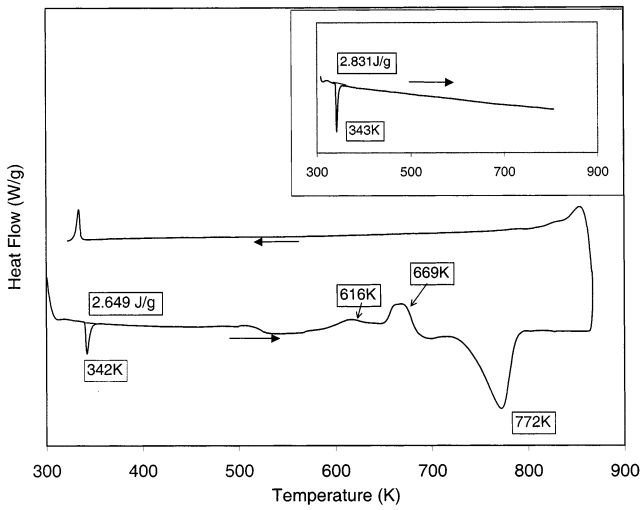

Figure 3. DSC curve $x = 9$ at a heating rate of 15 K/min. Direction of arrows gives the direction of heating. Inset shows the second run of the DSC scan already exposed to the DSC cycle.

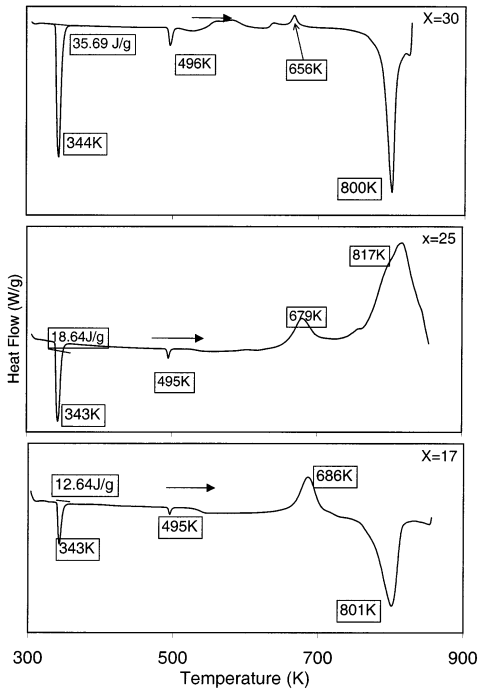

Figure 4. DSC curve $(V_2O_5)_{100-x}Se_x$ ($x = 17$, 25, 30) at a heating rate of 15 K/min. Direction of arrows gives the direction of heating.

fraction of elemental Se present in the sample. Also, in the present temperature range, peaks not assigned to the monoclinic−tetragonal phase transition of VO_2 appear irreversible for $x \geq 17$. The results for the DSC curves are tabulated in Table 2. A comparison of the areas under the curve assignable to the melting of Se and the transition in VO_2 is also provided in Table 2. In these cases, the area is reported relative to the mass of the total sample; thus, an increase in the area (i.e., J/g) indicates an increase in the component of the mixture relative to the total mass. The data indicate that an increase in the selenium content, x, from 9 to 30 promotes the formation of both VO_2 and isolated Se particles; that is to say that the miscibility of each in the quenched material decreases with increasing x. Large irreversible endothermic peaks were observed for

Table 2. Thermal Parameters Obtained from the DSC Curve for the as-Prepared Samples, Heated at 15 K/min[a]

	as prepared				
$x =$ wt %	T_{M-T} (K)	A_{M-T} (J/g)	T_{mSe} (K)	A_{Se} (J/g)	$(A_{Se}/A_{M-T}) \times 10^{-2}$
9	342	2.6			
17	343	12.6	495	0.9	7.3
25	343	18.6	495	1.3	6.8
30	344	35.7	497	3.5	9.8

[a] Here, T_{M-T} represents the peak temperature to monoclinic-tetragonal (M−T) transformation, A_{M-T} the area under the curve for the M−T transformation, T_{mSe} the melting temperature for the selenium, and A_{Se} the area under the peak for the selenium melting peak. The literature value for the melting point of selenium is 494 K.

samples with $x = 9$, 17, and 30 at 772, 800, and 801 K, respectively, while a large irreversible exothermic peak was observed at 817 K for a sample with $x = 25$. At this stage, we are unable to completely explain the presence of irreversible peaks observed in the DSC scan. One of the possibilities could be the presence of V_6O_{13} that has a lower melting point than V_2O_5.[35] Near its melt temperature, V_6O_{13} may be undergoing decomposition/desorption or some chemical reaction with other sample constituents. This hypothesis is supported by the fact that in the cooling curve we do not observe any peaks other than the monoclinic to tetragonal transition.

Dielectric Studies. In DEA measurements capacitance and conductance were calculated according to eqs 1 and 2[27]

$$C(\text{farads}) = \frac{I_{\text{measured}}}{V_{\text{applied}}} \times \frac{\sin\theta}{2\pi f} \tag{1}$$

$$\frac{1}{R}(\text{ohm}^{-1}) = \frac{I_{\text{measured}}}{V_{\text{applied}}} \times \cos\theta \tag{2}$$

where R is the resistance (ohms), I the current, V the voltage, f the applied frequency (Hz), and θ the phase angle shift between applied voltage (V_{applied}) and measured current (I_{measured}). For parallel plate electrodes, permittivity (e') and loss factor (e'') were calculated by

$$e' = \frac{Cd}{e_0 A} \tag{3}$$

$$e'' = \frac{d}{RA2\pi f e_0} \tag{4}$$

A is the electrode plate area, d the plate spacing, and e_0 the absolute permittivity of free space (8.85×10^{-12} F/m). Figure 5 shows the room-temperature frequency dependence of permittivity for $(V_2O_5)_{100-x}Se_x$ samples. The positive values of permittivity are represented by (▲) and the negative values by (◆). For samples where $x = 9$, the permittivity decreased with an increase in frequency, changing from negative to positive values at ≈4 Hz. At higher frequency (1 kHz to 10 kHz) large resonance-type oscillations were observed. The permittivity also switched from positive to negative and back to positive values at around 7−8 kHz. However, lack of sufficient data points for this flip-flop behavior adds

(35) Silva, I. F.; Palma, C.; Klimkiewicz, M.; Eser, S. *Carbon* **1998**, *36*, 861.

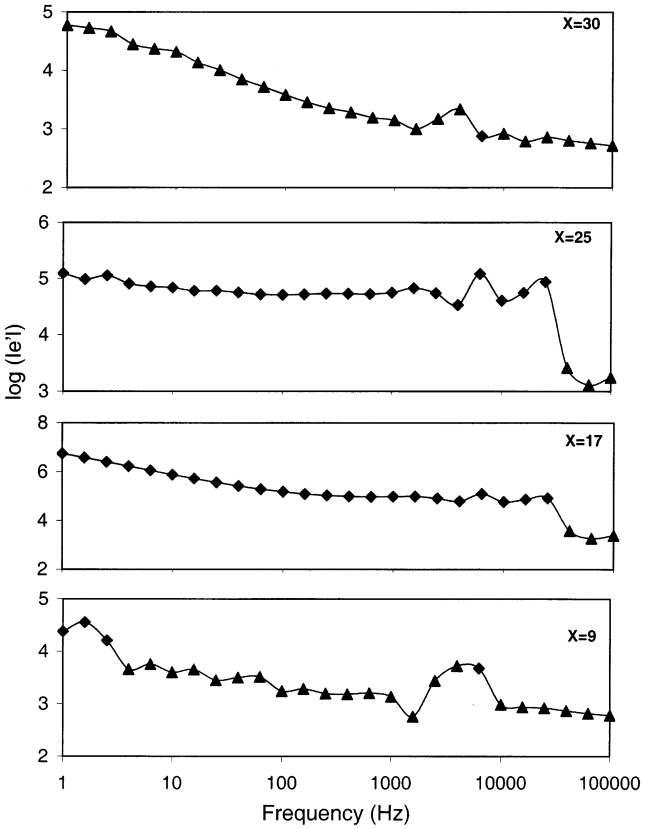

Figure 5. Room-temperature variation of permittivity as a function of applied frequency for $9 \leq x \leq 30$. Values of permittivity and frequency are plotted on a log scale. The positive values of permittivity are represented by (▲) and the negative values by (◆).

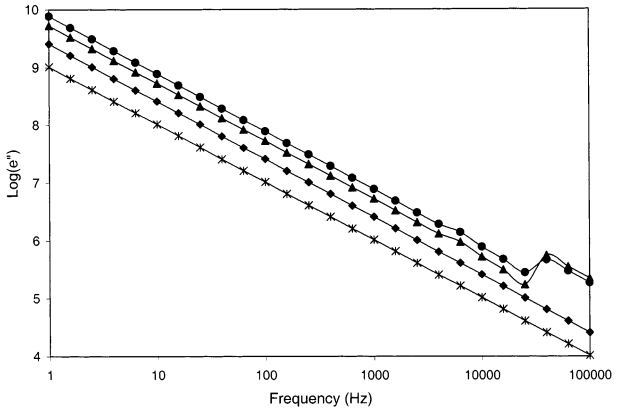

Figure 6. Variation of loss factor as a function of applied frequency for (◆) $x = 9$, (▲) $x = 17$, (●) $x = 25$, and (*) $x = 30$ at room temperature. Values of loss factor and frequency are plotted on a log scale.

uncertainty to the presence of this feature. The permittivity for $x = 17$ and 25 remained negative over a large frequency range, decreasing with increasing frequency. However, the permittivity for $x = 17$ and 25 changed from negative to positive values at 25.1 kHz. We observed only positive permittivity values for $x = 30$, with an exception at only one frequency, and the permittivity decreased with the increase in frequency. The resonance-type oscillations were also present at higher frequencies for samples where $9 < x = 30$.

Figure 6 shows the variation of loss factor as a function of frequency at room temperature. For samples with $x = 9$ and 30, the curve for log(loss factor) vs log-

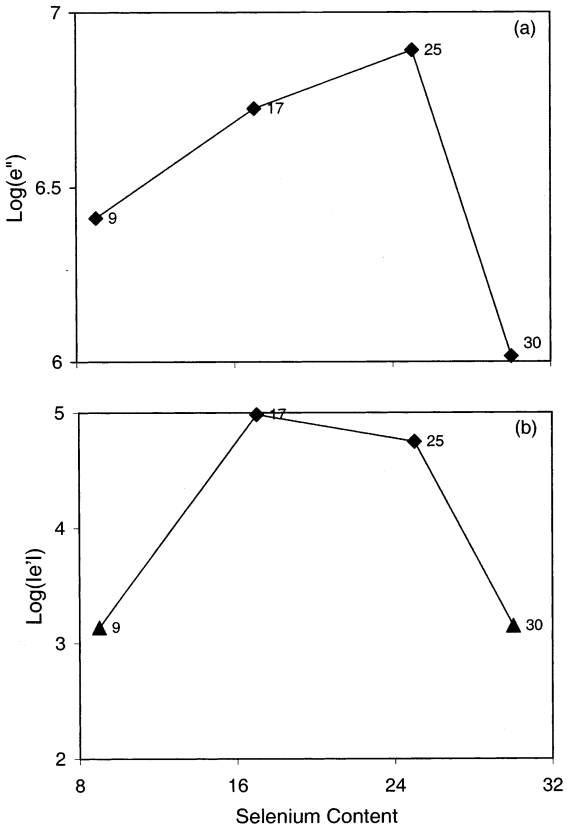

Figure 7. Variation of (a) loss factor and (b) permittivity as a function of composition, for a fixed frequency of 1 kHz at room temperature. The positive values of permittivity are represented by (▲) and the negative values by (◆).

(frequency) remained linear over the entire applied frequency range. However, for samples with $x = 17$ and 25, the values of the loss factor changed by a factor of 4 and 3, respectively, at a frequency of 25.1 kHz. As seen in the figure, there was a sudden increase in the value of the resistive component at 25.1 kHz for $x = 17$ and 25. Also, the capacitance for samples with $9 < x < 30$ underwent a transformation from positive to negative values at this value of frequency. While the sample $x = 9$ also showed transformation from negative to positive values of permittivity at 3 Hz, this sudden increase in the resistive component was absent in the current frequency range for this sample. Hence, the resistive component is clearly not the driving force behind the transformation from positive to negative values of permittivity as a function of frequency. The values of the room-temperature loss factor and permittivity as a function of composition, at 1 kHz, are plotted in Figure 7.

One model that may explain the presence of overall negative permittivity in the melt-quenched $(V_2O_5)_{100-x}Se_x$ alloys and its frequency response should take into consideration the presence of various V−O, Se, and Se−O phases and their relative concentration within the quenched melt. This assumption complicates any attempt to model the present system. At this point, we have not made an attempt to propose such a model. Also it is to be noted that there is not a satisfactory theory to completely explain the occurrence of negative permittivity or capacitance in several classes of materials and systems.[36] In the past, the origin of negative capacitance at high frequency had been attributed to the inductive contribution of the external electric circuit.[18] However,

in the present case, the negative capacitance has not only been observed at low frequencies but also appears to be a function of selenium content. The presence of negative permittivity in V_2O_5-Se alloys can be qualitatively explained in terms of the ionization model for negative capacitance in low-mobility semiconductors such as amorphous chalcogenides,[37] assuming the presence of small selenium crystallites dispersed within the vanadium oxide matrix. With the application of applied voltage, the selenium crystallites dispersed in the vanadium oxide phase, by virtue of their small crystallite size, may experience electric fields high enough to provide excess carriers by impact ionization. Since the room-temperature hole mobility for selenium ($\mu^h \sim 0.14$ cm^2/Vs)[38] is much greater than the electron mobility ($\mu^e \sim 5 \times 10^{-3}$ cm^2/Vs),[39] a lag of the current behind voltage occurs. This lag yields a negative contribution to the ac capacitance. With an increase in the selenium content to $x = 17$, the number of these small selenium crystallites present in the vanadium oxide matrix increases, causing the values of permittivity to increase. This reasoning is in line with the XPS data where the ratio of Se/SeO_2 increased from 0.05 for $x = 9$ to ~0.4 for $x = 17$ and remains approximately the same for $x = 25$ and $x = 30$. However, upon further increase of selenium content, larger selenium crystallites were likely formed, causing the weakening of the localized electric fields. Thus, the negative capacitance, hence, permittivity, decreased with reduced field as the impact ionization coefficient decreased.[37] For samples with $x = 30$, due to large selenium crystallite sizes, the electric field at the interface decreased enough to prevent the carrier generation by impact ionization.

Allen et al.[20] had noted that the negative capacitance effects (related to permittivity by eq 3) in chalcogenide glasses were intimately connected to the electrical switching phenomena in amorphous semiconductors. It has also been seen for $Al-V_2O_5-Al$ devices that the temperature at which the capacitance becomes negative decreases as the device temperature increases.[21] Thermal dependence of permittivity measured on $BaTiO_3$ and $BaFe_{12}O_{19}$ indicates an increase in the values of negative permittivity with increased temperature.[40]

The variation of normalized permittivity as a function of temperature in the range 273−373 K, at a fixed frequency of 1 kHz, is shown in Figure 8. The arrows in the figures indicate the direction of the heat flow (i.e., heating and cooling). The normalized permittivity is defined as the ratio of permittivity at temperature T and permittivity at 273 K (e'_T/e'_{273K}). As seen in Figure 8, the values of permittivity also show the reversible transition across the temperature-induced semiconductor to metal transition. Samples where $x = 9$ showed a positive value of permittivity at 1 kHz at 273 K. However, as the sample was heated above room temperature, it exhibited a transformation from positive to negative values of permittivity at ≈349 K following the semiconductor to metal transformation. The absolute value of negative permittivity increased with increased

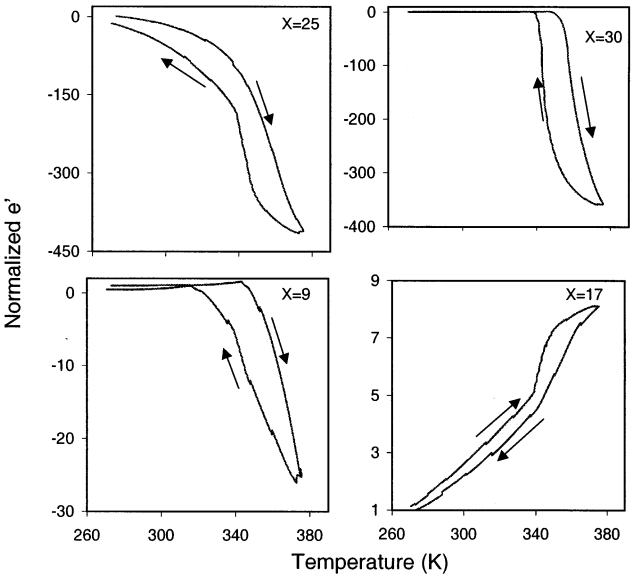

Figure 8. Values of normalized permittivity, at a fixed frequency of 1 kHz, as a function of temperature in the range $273 \leq T \leq 373$ K are shown for $x = 9, 17, 25, 30$. Normalized permittivity is defined in the text. Note the change in the positive to negative values.

temperature. Permittivity for $x = 17$ remained negative throughout the current temperature range, with its absolute value increasing with increased temperature. The sample where $x = 25$ exhibited a positive value of permittivity at 1 kHz at 273 K. However, as this sample was heated above ≈277 K, it exhibits transformation from positive to negative values of permittivity, the absolute value of negative permittivity increasing with increased temperature. Sample $x = 30$ showed positive values of permittivity at 273 K. However, this sample also showed a transformation from positive to negative values of permittivity at ≈338 K, in the same temperature range where the semiconductor to metal transformation occurs. These results clearly indicate that, in some of our samples ($x = 9, 30$), semiconductor to metal transformation plays an important role in the temperature-induced transformation from positive to negative values of permittivity. However, the absence of this switching for $x = 17$ in the present temperature regime and presence of this switching at a temperature far below the semiconductor to metal transition for $x = 25$ is not clear. It seems that there must be other factors also responsible for this switching. It was found that among all the samples studied, the sample where $x = 30$ showed a change in the value of absolute permittivity by 2 orders of magnitude with a minimum temperature range of hysteresis.

Also, as seen in Figure 8, only the monoclinic to tetragonal transformation for samples where $x = 9$ and $x = 30$ was sharp, while that for $x = 17$ and $x = 25$ was relatively broad. It seems that the presence of elemental Se decreased the sharpness of the changes in the permittivity values across the monoclinic to tetragonal transformation. However, the increased presence of VO_2 is likely to facilitate the sharp changes in the permittivity values across the monoclinic to tetragonal transformation. Hence, the features seen in Figure 8 are likely a result of competing processes between that of the selenium that disrupts the abrupt permittivity changes and that of the VO_2 phase, which facilitates the

(36) Gutierrez, F. F.; Ruiz-Salvador, A. R.; M'Peko, J. C.; Velez, M. H. *Europhys. Lett.* **1998**, *44*, 211.
(37) Rockstand, H. K. *J. Appl. Phys.* **1971**, *42*, 1159.
(38) Spear, W. E. *Proc. Phys. Soc. (London)* **1960**, *76*, 826.
(39) Mikla, V. I. *Phys. Status Solidi A* **1998**, *165*, 427.
(40) M'Peko, J.-C. *Appl. Phys. Lett.* **2000**, *77*, 735.

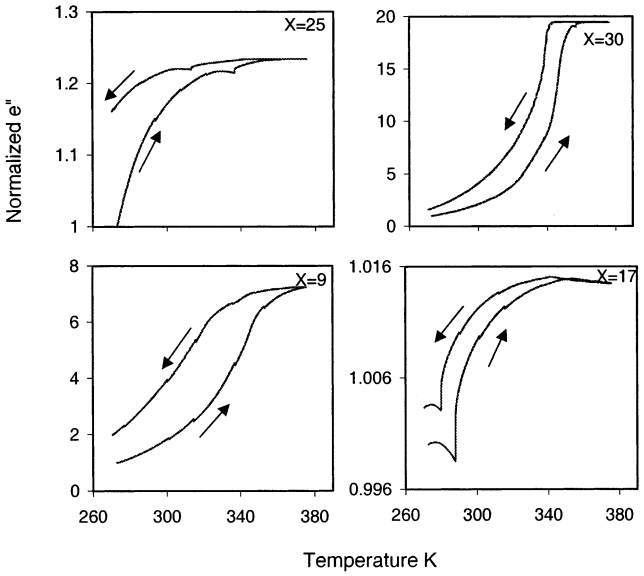

Figure 9. Values of normalized loss factor, at a fixed frequency of 1 kHz, as a function of temperature in the range $273 \leq T \leq 373$ K are shown for $x = 9, 17, 25, 30$. Normalized loss factor is defined in the text. Note the decrease in loss factor with increase in the temperature around the monoclinic−tetragonal transformation for $x = 17$.

abrupt changes in the permittivity values across the monoclinic to tetragonal transformation.

Figure 9 shows the variation of normalized loss factor as a function of temperature in the temperature range 273−373 K, at a fixed frequency of 1 kHz. The normalized loss factor is defined as the ratio of loss factor at temperature T to the loss factor at 273 K (e''_T/e''_{273K}). The arrows in the figures indicate the direction of the heat flow. These variations indicate that the sample with $x = 30$ shows a large reversible change in loss factor across the monoclinic to tetragonal phase transition with a minimum temperature range of hysteresis. The monoclinic to tetragonal phase transition in VO_2 is a semiconductor to metal transition. Hence, below the transition temperature, following the conductivity of semiconductors, the resistivity of alloys is expected to decrease with increased temperature, leading to an increase in the loss factor at higher temperatures following eq 4 (ignoring changes in d and A). Indeed, this trend is clearly evident for all the samples in the current experimental range. However, after the transition temperature, following the conductivity of metals, the resistivity of alloys is expected to increase with increased temperature, leading to a decrease in the loss factor at higher temperatures. As seen in the figure, this effect was only seen in the sample with $x = 17$ after the transition temperature. It is to be noted that all the samples also comprise Se, Se−O, and V−Se phases along with V−O compounds. Therefore, the net change in the resistivity of the sample is a sum total of the temperature-dependent resistivity changes of all its constituents. At this stage, no attempt has been made to quantify the contribution of individual constituents to the total change in the resistivity of the samples.

Diffuse Reflectance Measurements. Diffuse reflectance measurements at room temperature in the wavelength range 250−1000 nm were carried out on the samples. The reflectivity values at 750 nm for $x = 9$, 17, 25, and 30 were 20, 11, 16, and 26%, respectively, while for standard Se, V_2O_5, and SeO_2 at 750 nm were 13, 74, and 75%, respectively.

As seen, with the addition of selenium into the melt, reflectivity decreased until $x = 17$; thereafter, it increased with further addition of selenium to $x = 30$. As seen in Figure 1, (010) and (020) reflections from V_2O_5 are absent in the XRD pattern for the sample with $x = 17$. However, these peaks appeared in the patterns for $x = 25$ and 30. It was also observed from the XRD patterns that the V_2O_5 fraction increased with a concomitant increase in selenium from $x = 25$ to $x = 30$. As seen in Table 1, the ratio of Se/SeO_2 in the $x = 9$ was 0.05, while for other samples it was ≈0.4. Also, the ratio of SeO_2/V_2O_5 follows the XRD trend for V_2O_5; the ratio increased with initial addition of selenium and decreased with further addition of selenium for $x > 17$. Hence, the reflectivity values observed were a sum total of contribution from Se, V_2O_5, and SeO_2 and other components (V_6O_{13}). Since the absolute diffuse reflectivity values of $V_2O_5 \sim SeO_2 \gg Se$, the initial decrease in the reflectivity values for $x = 17$ is likely due to the absence of the V_2O_5 phase. Also, the absolute amount of SeO_2 in the sample with $x = 17$ was not high enough to compensate for the loss of reflectivity due to the absence of V_2O_5. For samples with $x = 25$ and $x = 30$, the presence of an increased presence of V_2O_5 along with SeO_2 caused the increase in the values of reflectivity, with the absolute amount of SeO_2 in the sample likely to be higher in the sample with $x = 30$.

Conclusions

Melt-quenched $(V_2O_5)_{100-x}Se_x$ ($9 \leq x \leq 30$) alloys have been well-characterized by XRD, XPS, DSC, DEA, and optical absorption spectroscopy. Negative permittivity is seen in samples with $x < 30$. The presence of negative permittivity in V_2O_5−Se alloys as a function of selenium content is qualitatively explained in terms of the ionization model for negative capacitance in low-mobility semiconductors. With the application of applied voltage, the small selenium crystallites dispersed in vanadium oxide phase experience electric field high enough to provide excess carrier by impact ionization. Since the room-temperature hole mobility for selenium is much greater than the electron mobility, a lag of the current behind voltage occurs, which gives a negative contribution to the ac capacitance. The qualitative changes in the value of permittivity are explained in terms of the presence of small selenium crystallites whose number and crystallite size increase with the increasing selenium content. The changes in the permittivity and loss factor are reversible across the monoclinic to tetragonal transformation with $x = 30$ exhibiting the minimum temperature range of hysteresis and maximum change in the values of permittivity. In some of our samples ($x = 9$, 30), semiconductor to metal transformations play an important role in the temperature-induced transformation from positive to negative values of permittivity.

Acknowledgment. The authors would like to acknowledge the financial support provided by the National Science Foundation Grant NSF-DMR-0076180 and instrument Grant NSF-CHE-9808024 and CHE-9977398. Acknowledgments are also due to Dr. C. Chusei for support with XPS data acquisition.

CM011574L